Eur. J. Biochem. **269**, 2040–2051 (2002) © FEBS 2002 doi:10.1046/j.1432-1033.2002.02852.x

Electrostatic properties of the structure of the docking and dimerization domain of protein kinase A IIα

Dimitrios Morikis[1], Melinda Roy[2], Marceen G. Newlon[2], John D. Scott[3] and Patricia A. Jennings[2]

[1]*Department of Chemical and Environmental Engineering, University of California at Riverside, Riverside, USA;*
[2]*Department of Chemistry and Biochemistry, University of California at San Diego, La Jolla, USA;*
[3]*Howard Hughes Medical Institute, Vollum Institute, Portland, OR, USA*

The structure of the N-terminal docking and dimerization domain of the type IIα regulatory subunit (RIIα D/D) of protein kinase A (PKA) forms a noncovalent stand-alone X-type four-helix bundle structural motif, consisting of two helix-loop-helix monomers. RIIα D/D possesses a strong hydrophobic core and two distinct, exposed faces. A hydrophobic face with a groove is the site of protein–protein interactions necessary for subcellular localization. A highly charged face, opposite to the former, may be involved in regulation of protein–protein interactions as a result of changes in phosphorylation state of the regulatory subunit. Although recent studies have addressed the hydrophobic character of packing of RIIα D/D and revealed the function of the hydrophobic face as the binding site to A-kinase anchoring proteins (AKAPs), little attention has been paid to the charges involved in structure and function. To examine the electrostatic character of the structure of RIIα D/D we have predicted mean apparent pK_a values, based on Poisson–Boltzmann electrostatic calculations, using an ensemble of calculated dimer structures. We propose that the helix promoting sequence Glu34-X-X-X-Arg38 stabilizes the second helix of each monomer, through the formation of a (i, $i+4$) side chain salt bridge. We show that a weak inter-helical hydrogen bond between Tyr35–Glu19 of each monomer contributes to tertiary packing and may be responsible for discriminating from alternative quaternary packing of the two monomers. We also show that an inter-monomer hydrogen bond between Asp30–Arg40 contributes to quaternary packing. We propose that the charged face comprising of Asp27-Asp30-Glu34-Arg38-Arg40-Glu41-Arg43-Arg44 may be necessary to provide flexibility or stability in the region between the C-terminus and the interdomain/autoinhibitory sequence of RIIα, depending on the activation state of PKA. We also discuss the structural requirements necessary for the formation of a stacked (rather than intertwined) dimer, which has consequences for the orientation of the functionally important and distinct faces.

Keywords: PKA; AKAP; NMR; dimer; pK_a.

Protein phosphorylation controls many cellular processes including carbohydrate metabolism, muscle contraction, lymphocyte activation, secretion and cell growth, differentiation and apoptosis. Activation of protein kinases and phosphatases is an integral component in the signaling pathways that mediate these cellular processes. This activation is triggered by specific hormones with the aid of second messengers, including Ca^{2+}, phospholipids, or cAMP. In turn, protein kinases or protein phosphatases alter the phosphorylation state of specific subcellular targets [1]. Because many protein kinases are of broad specificity, a key question has been how these enzymes mediate specific events in the appropriate time frame. It is now apparent that subcellular localization of kinases near their preferred targets affords this control. This localization and selective phosphorylation and dephosphorylation of protein targets in the cell are mediated by specific protein–protein interactions [2,3]. The cAMP-dependent protein kinase (PKA) is tethered to specific subcellular compartments by A-Kinase Anchoring Proteins (AKAPs). The site of interaction with AKAPs is the N-terminal docking and dimerization (D/D) domain of the regulatory (R) subunit of PKA. While early studies indicated that only the type IIα regulatory subunits are targeted, the recent discovery of dual-specificity AKAPs (D-AKAPs) indicates that the type I enzyme may also be localized [4].

The N-terminal dimerization domain of the Type IIα regulatory subunit of PKA, called hereafter RIIα D/D, possesses two solvent exposed faces with distinct structural properties. One face is highly hydrophobic with a well-understood function as the AKAP binding site [5,6]. The other face is highly charged and has not been the subject of detailed study. The hydrophobic and charged faces of the RIIα D/D are diametrically opposed to each other. Interestingly, phosphorylation of RIIα by the cyclin B-p34^{cdc2} kinase (CDK1) just outside the D/D alters the subcellular localization of RIIα at the onset of mitosis [7]. Thus, the electrostatic environment influences the affinity of

Correspondence to D. Morikis, Department of Chemical and Environmental Engineering, University of California at Riverside, Riverside, CA 92521-0444, USA. Fax: + 1 909 787 5696, Tel.: + 1 909 787 2696, E-mail: dmorikis@engr.ucr.edu, or P. A. Jennings Department of Chemistry and Biochemistry, University of California at San Diego, La Jolla, CA 92093-0359, USA. E-mail: pajennin@ucsd.edu

Abbreviations: PKA, cAMP-dependent protein kinase or protein kinase A; R, regulatory; C, catalytic; D/D, docking and dimerization; AKAP, A-kinase-anchoring protein.

(Received 4 October 2001, revised 6 February 2002, accepted 16 February 2002)

RIIα for its anchoring partner, suggesting communication between the diametrically opposed functional faces. To examine the electrostatic properties of RIIα D/D, we have applied a Poisson–Boltzmann continuum electrostatics method on an ensemble of calculated solution structures, which has led to prediction of mean apparent pK_a values of all ionizable residues of RIIα D/D. The use of the ensemble of NMR structures is more suitable for the calculation because it provides us with a range of pK_a values, from structures that comply with the permitted conformational space, but allow for flexibility as indicated by their rmsd. We have used a two-step molecular dynamics/simulated annealing protocol with NMR restraints, to determine the ensemble of structures of RIIα D/D. Initial monomer RIIα D/D structures were calculated using a subset of NOEs determined to be unambiguous intra-monomer NOEs. Subsequently, the coordinates of the monomer structures were used as starting structures for the dimer calculations, using the complete set of available NOEs. This protocol allows for the investigation of the role of electrostatics in guiding the optimum relative topology of the two monomers of the dimer. Using the pK_a values and structural arguments, we have determined the role of charges in interactions associated with secondary, tertiary, and quaternary structure packing and stability. In addition, we discuss the role of charges in function of RIIα D/D.

MATERIALS AND METHODS

Sample preparation and NMR spectroscopy

Sample preparations and the types of experiments and conditions used have been described previously [5,6,8]. The sample pH was 4.

Conversion of NMR parameters to structural restraints

Spectral processing, cross peak picking and volume integrations were performed using the program FELIX 95 (Molecular Simulations). NOE volumes were measured using the 2D ^{1}H-^{1}H NOESY (τ_m = 100 and 200 ms), 3D ^{1}H-^{15}N NOESY-HSQC (τ_m = 150 ms), 3D ^{1}H-^{13}C HMQC-NOESY (τ_m = 150 ms), and 3D ^{13}C-edited (ω_2), ^{12}C-filtered (ω_1)/^{13}C-filtered (ω_3) NOESY (τ_m = 150 ms), collected at 25 °C [5,8]. The NOE volumes were calibrated using known averaged or fixed distances. Cross peaks in helical segments were used as reference for calibration and they were H_α-H_N (i, i + 3) (3.4 Å) for the 2D ^{1}H-^{1}H NOESY and the 3D ^{1}H-^{15}N NOESY-HSQC, H_α-H_β (i, i + 3) (3.4 Å) for the 3D ^{1}H-^{13}C HMQC-NOESY and by visual inspection for the 3D ^{13}C-edited (ω_2)-^{12}C-filtered (ω_1)/^{13}C-filtered (ω_3) NOESY. An NOE-derived distance restraint list was generated within the program FELIX 95 using the following classification: strong NOEs (1.8 Å $\leq r_{ij} \leq$ 2.7 Å, where r_{ij} is the interproton distance between protons i,j), medium NOEs (1.8 Å $\leq r_{ij} \leq$ 3.3 Å), weak NOEs (1.8 Å $\leq r_{ij} \leq$ 5.0 Å) and very weak NOEs (1.8 Å $\leq r_{ij} \leq$ 6.0 Å). The upper boundary of NOEs involving amide protons was extended by 0.2 Å to account for the higher observed intensity of this type of cross peaks. In addition, a correction of 0.5 Å was added to the upper boundaries of the distances involving methyl groups to account for the averaging of the three methyl protons. During structure calculations, distances involving non-stereospecifically assigned or degenerate methylene protons and methyl groups were incorporated as $(\Sigma r^{-6})^{-1/6}$ 'effective distances' [9,10].

$^3J_{HN\text{-}H\alpha}$-coupling constants were measured from a 3D HNHA spectrum by measuring the intensity ratio of cross peaks to diagonal peaks for resolved ^{15}N-^{1}H pairs. $^3J_{HN\text{-}H\alpha}$-coupling constants were converted to ϕ-dihedral angle restraints as follows: $\phi = -60° \pm 30°$, for $3 < {}^3J_{HN\text{-}H\alpha} < 5.5$ Hz and presence of sequential NOE connectivities consistent with an α helix, $\phi = -140° \pm 40°$ for $8 < {}^3J_{HN\text{-}H\alpha} < 9$ Hz, and $\phi = -140° \pm 30°$ for $^3J_{HN\text{-}H\alpha} > 9$ Hz for the β strand/random coil region. A total of 25 ϕ-dihedral angle restraints per monomer were used. Residue Ile5 was assigned to a restraint $\phi = -90° \pm 90°$, because spectral overlap did not allow an accurate determination of the coupling constant.

Side chain χ_1-dihedral angles for Val18, Val20, Val29, Val33 and Thr37 were restricted to one of the staggered conformations, which was in all cases −60° with an associated error of ± 30°. These values were deduced using the combined information of the intensities of $J_{\alpha\beta}$ couplings from the 2D DQF-COSY spectrum and the NOE intensities of the HN-H_β and H_α-H_β cross peaks from the 2D and 3D NOESY spectra. A total of 5 χ_1-dihedral angle restraints per monomer were used. Using the same information stereospecific methyl assignments for the above mentioned valines were made.

Intra-monomer backbone hydrogen bond restraints were used in the final stages of the structure calculations for parts of the secondary structure that were well-defined α helices as indicated by the combined information of sequential NOE connectivities H_α-H_N (i,i + 1; i,i + 2; i,i + 3; i,i + 4), H_α-H_β (i,i + 3), $^3J_{HN\text{-}H\alpha}$-coupling constants in the region $3 < {}^3J_{HN\text{-}H\alpha} < 5.5$ Hz and protection from hydrogen exchange [8]. The hydrogen bond restraints were introduced in the structure calculations as distance restraints of 3.3 Å (lower limit 2.5 Å, upper limit 3.5 Å) for O-N, and 2.3 Å (lower limit 1.5 Å, upper limit 2.5 Å) for O-HN. A total of 19 hydrogen bond restraints per monomer were used.

Monomer structure calculations

The RIIα D/D monomer structures were calculated using the program X-PLOR 3.851 [11]. The hybrid distance geometry-simulated annealing and refinement protocol [12] was utilized (DG_SUB_EMBED, DGSA, REFINE, using an initial template random structure with good local geometries and no nonbonded contacts). A total of 457 NOE-derived distance restraints were used (Table 1). The minimization target function during simulated annealing was composed of quadratic harmonic potential terms for covalent geometry (bonds, angles, planes, chirality), quadratic square-well potentials for the experimental distance and dihedral angle restraints, and a quartic van der Waals repulsion term for the nonbonded contacts [11]. No explicit hydrogen bonding, electrostatic or 6–12 Lennard-Jones potential energy terms were used in the simulated annealing target function. A quadratic distance geometry term was minimized during coordinate regularization [11]. The input force constants for bonds, angles, planes, and chirality were 1000 kcal·mol^{-1}·Å^{-2}, 500 kcal·mol^{-1}·rad^{-2}, 500 kcal·mol^{-1}·rad^{-2}, 500 kcal·mol^{-1}·rad^{-2}, respectively, 4 kcal·

Table 1. RIIα D/D structure determination statistics: NMR restraints.

Monomer structure calculation	
Total NOE	457
Intra-residue ($i - j = 0$)	185
Sequential ($\|i - j\| = 1$)	136
Medium range ($1 < \|i - j\| \leq 4$)	95
Long range ($\|i - j\| > 4$)	41
Hydrogen bond	19
Total dihedral angle	30
ϕ	25
χ_1	5
Dimer structure calculation [a]	
Total NOE	505
Intra-residue ($i - j = 0$)	185
Sequential ($\|i - j\| = 1$)	136
Medium range ($1 < \|i - j\| \leq 4$)	95
Long range ($\|i - j\| > 4$)	25
Inter-monomer	38
Ambiguous	26
Hydrogen bond	19
Total dihedral angle	30
ϕ	25
χ_1	5

[a] Restraints per monomer.

$mol^{-1}\cdot rad^{-4}$ for the quartic van der Waals repulsion term, 50 $kcal\cdot mol^{-1}\cdot Å^{-2}$ for experimental NOE restraints, and 200 $kcal\cdot mol^{-1}\cdot rad^{-2}$ for experimental dihedral angle restraints. Force constants were varied during the structure calculations according to the standard X-PLOR protocols [11].

Dimer structure calculations

The RIIα D/D dimer structures were calculated using the program X-PLOR and a protocol developed by the group of M. Nilges (MDSA-SO-WDMR-1.0) [13,14]. The dynamic NOE assignment method of Nilges [10] was used to calculate an 'effective distance' comprising of the sum of the intra- and inter- monomer distances $[(\Sigma r^{-6})^{-1/6}$ averaging per monomer]. The initial structures were the accepted monomer structures. The minimization target function potential terms for covalent geometry, van der Waals repulsion, experimental intra-residue NOEs and dihedral angles were the same as in the monomer calculation. In addition soft-square potential terms were used for experimental inter-monomer and ambiguous NOEs, a symmetry soft-square potential term was used for global symmetry NOEs, a quadratic harmonic potential term was used for noncrystallographic symmetry (NCS) restraints and a quadratic harmonic potential term was used for packing to prevent monomers from drifting apart. The input force constants were as in the monomer calculation for covalent geometry terms, the van der Waals repulsion term and the experimental dihedral angle term. The input force constants were 50 $kcal\cdot mol^{-1}\cdot Å^{-2}$ for intra-monomer, inter-monomer, and ambiguous NOEs, 2 $kcal\cdot mol^{-1}\cdot Å^{-2}$ for symmetry NOEs, 2 $kcal\cdot mol^{-1}\cdot Å^{-2}$ for NCS restraints, and 0.3×10^{-6} $kcal\cdot mol^{-1}\cdot Å^{-2}$ for packing. Force constants were varied during the structure calculations according to the standard X-PLOR protocol [13]. A total of 505 NOE-derived distance restraints were used (Table 1).

pK_a calculations

The method of Antosiewitz *et al.* [15,16], implemented within the program UHBD [17,18] was used for the calculations of pK_a values of the NMR ensemble of structures of RIIα D/D. Poisson–Boltzmann continuum electrostatic calculations were performed to calculate electrostatic potentials, which were used for determination of differences in the ionization free energy ($\Delta\Delta G$) of the charged and neutral forms of each ionizable site in the protein and free in solution. Then, intrinsic pK_a values of each ionizable site were computed using $\Delta\Delta G$ values and experimental model pK_a values, as described in Antosiewitz *et al.* [15]. Apparent pK_a values for each ionizable site of RIIα D/D were calculated, taking into account interactions among all ionizable sites in their ionized states, using the 'clustering' method of Gilson [19]. Finally, mean pK_a values and their rmsds were calculated using the 24 NMR structures of our final ensemble of dimer structures of RIIα D/D.

Dielectric smoothing at the protein–solvent interface [20,21] was used, with an ion exclusion layer around the protein defined by a probe of 2.0-Å radius. Finite difference focusing methods [22,23] were used in the calculations, with focusing grids of 2.5, 1.25, 0.5, and 0.25 Å. The parameter set of charges and van der Waals radii PARSE [24], dielectric constants of 78.4 and 20.0, for solvent and protein, respectively, temperature of 298 K, and ionic strength corresponding to 100 mM were used. Justification for the relatively high value of the protein dielectric constant is discussed in Antosiewitz *et al.* [15,16]. Changes from the neutral to charged ionization state, were made by adding a $\pm$ 1 charge to each ionizable site, depending on their charge. Negative unit charges were added at the following atoms: C_t of the C-terminus, C_γ of Asp and C_δ of Glu, and O_η of Tyr. Positive unit charges were added at the following atoms: N_t of the N-terminus, N_ζ of Lys, C_ζ of Arg, and N_δ or N_ε of His (depending on the position of the initial hydrogen in the neutral form). The initial protonation and flip state of His, and flip state of Asn and Gln residues, was established using the global hydrogen bonding network optimization option of the program WHAT IF vs. 99 [25,26]. Addition of hydrogens to establish the neutral state of Asp and Glu residues, at the $O_{\delta 2}$ and $O_{\varepsilon 2}$ atoms, respectively, was made using a special version of WHAT IF provided to us by J. E. Nielsen & G. Vriend (EMBL and University of Nijmegen). The experimental model pK_a values used were: 12.0 for Arg, 10.4 for Lys, 9.6 for Tyr, 6.3 for His, 4.4 for Glu, 4.0 for Asp, 7.5 for the N-terminus, and 3.8 for C-terminus.

Structure validations and molecular graphics

Structures were visually inspected using the program MOLMOL [27]. The programs PROCHECK-NMR [28] and WHAT IF [26] were used for structure validation. The program MOLMOL [27] was used for secondary structure evaluation, solvent accessibility calculation, angular order parameters calculation, inter-helical angle calculation, and for protein structure figure preparation.

RESULTS

A total of 100 monomer structures of RIIα D/D were generated from a subset of our NMR NOE assignments, which were classified as unambiguous. From these initial calculations 49 monomer structures with no NOE violation > 0.3 Å, no dihedral angle violation > 5°, no bond violation > 0.05 Å, no angle violation > 5° and no improper angle violation > 5° were accepted, and used in subsequent dimer structure calculations. The total energies and the rmsds from the lowest energy structure of the 49 resulting dimer structures are plotted in increasing total energy value in Fig. 1. Dimer structures that showed NOE violations > 0.3 Å and/or dihedral angle violations > 5° are represented with open symbols in the plot. Most structures (41 out of 49; Fig. 1) with total energies 160–770 kcal·mol^{-1} and small rmsds from the lowest energy structure, converged to the same structural motif. This motif comprises two helix-turn-helix monomers packed in an antiparallel arrangement in a four-helix bundle with both helices (I and II) of monomer 1 on top of the respective helices (I′ and II′) of monomer 2. We call this stacked packing arrangement a top-top structure. A few structures (5 out of 49) with high total energy terms (890–2000 kcal·mol^{-1}), larger rmsds from the lowest energy structure, and with several NOE violations > 0.3 Å (up to 1 Å) have also been identified (Fig. 1). These structures possess a topology where helices I and II of monomer 1, and helices I′ and II′ of monomer 2, are intertwined. We call this a top-bottom structure. The inset of Fig. 1 shows a cylinder model of the lowest total energy structures of each of the two structural motifs, top-top and top-bottom. Both structural motifs pack into an X-type four-helix bundle, the difference between the two is the relative topology of the four helices. In addition, three ill-defined structures, different from each other, with the highest total energies (3900–8300 kcal·mol^{-1}) and the highest rmsds from the lowest energy structure were found (Fig. 1). These structures had several severe NOE violations > 0.3 Å (up to 1.6 Å) and/or dihedral angle violations > 5° (up to 11°). As the small ensemble of top-bottom structures and the three ill-defined structures suffer from significant experimental NOE or NOE and dihedral angle violations, we continued our analysis using the large ensemble of the top-top structures. Indeed we selected a subset of structures from the top-top ensemble (24 out of 41 structures) because some of the higher energy top-top structures also exhibited small NOE violations > 0.3 Å (up to 0.6 Å). The selected 24 structures form a continuous ensemble of lowest energy structures (in increasing energy value) that does not include any structure with restraint violations according to the criteria mentioned above (Fig. 1). This final ensemble, with cutoff total energy value at 240 kcal·mol^{-1}, comprising the 24 best RIIα D/D structures was used for further analysis (Fig. 1).

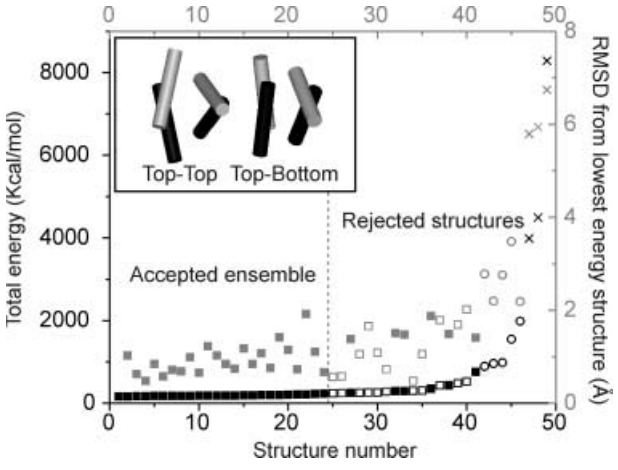

Fig. 1. Total energy plot of the 49 calculated dimer RIIα D/D structures. The structures are numbered in increasing energy order (black symbols). Forty-one structures conform with the top-top configuration (squares), five structures conform with the top-bottom configuration (circles) and three structures assume three different ill-defined configurations (×). Structures without NOE or dihedral angle violation are represented with solid symbols. Structures represented with open symbols possess NOE violations greater than 0.3 Å up to 1.6 Å. Structures #47 and #48 possess dihedral angle violations greater than 5° up to 11°. The vertical dashed line corresponds to the cutoff energy for the selection of the final ensemble of 24 structures with lowest energy and no NOE or dihedral angle violation (see text). Symbols drawn in grey represent the rmsd of each structure from the lowest energy structure (structure #1). The rmsds from the lowest energy structure are calculated by fitting the backbone atoms (N, Cα, C′) of residues 9–41. The inset shows a cylinder representation of the relative topology of the two different families of structures, top-top and top-bottom, found in the 49 calculated dimer structures of RIIα D/D. All top-bottom structures have significant NOE violations. The inset was generated using the program MOLMOL [27].

A superposition of the backbone of the final ensemble of 24 structures of RIIα D/D is shown in Fig. 2. The RIIα D/D homodimer consists of an antiparallel packing of the two subunits and possesses C_2 symmetry. Tables 2 and 3 summarize the structural statistics of the ensemble of 24 structures, the lowest energy and the best (smaller rmsd from the mean) structure of RIIα D/D. Each monomer of RIIα D/D consists of a disordered N-terminal segment

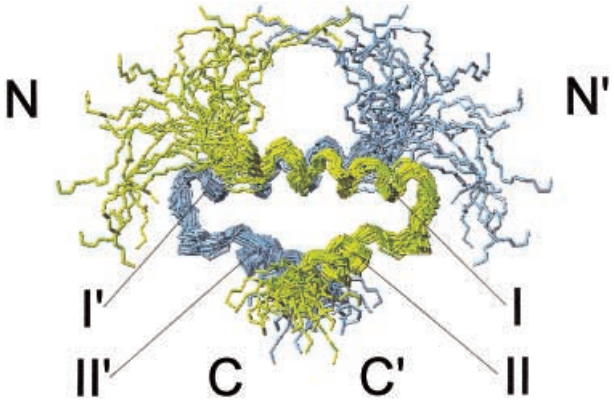

Fig. 2. Superposition of the ensemble of 24 calculated structures of RIIα D/D with lowest total energies. The structures are superimposed to minimize rmsds, by fitting the coordinates of the backbone heavy atoms (N, Cα, C′) between residues 9–41. Residues 9–41 contain the well-defined elements of secondary structure, helices I, II of monomer 1 (yellow traces) and helices I′, II′ of monomer 2 (grey traces). The location of the four helices and the amino and C-termini are indicated in the Figure. The Figure was generated using the program MOLMOL [27].

Table 2. RIIα D/D structure determination statistics: energetic analysis. Values are given in kcal·mol^{-1}.

Energy	Ensemble (24 structures)	Lowest energy structure	Best (closest to mean structure)[a]
Total	191.6 ± 18.3	163.6	178.6
Bond	5.7 ± 1.0	4.8	5.0
Angle	117.4 ± 5.3	110.4	114.7
Improper	15.3 ± 0.5	15.1	15.0
van der Waals	28.4 ± 8.5	14.9	27.5
NCS	2.3 ± 5.8	0.26	0.19
Packing	0.186 ± 0.008	0.188	0.197
Dihedral	0.006 ± 0.013	0.000	0.002
Total NOE	22.3 ± 5.6	17.9	16.0
Intra-residue NOE	21.3 ± 5.1	17.4	15.7
Inter-residue NOE	0.76 ± 1.00	0.36	0.27
Ambiguous NOE	0.13 ± 0.36	0.00	0.005
Symmetry NOE	0.11 ± 0.10	0.12	0.02

[a] The best structure was determined as the structure with the smallest rmsd from the mean structure by fitting the coordinates of the backbone heavy atoms (N, Cα, C′) between residues 9–41.

Table 3. RIIα D/D structure determination statistics: rmsds for the ensemble of 24 structures. Values are given in Å.

	rmsd from the mean		Pairwise rmsd	
Residues	Backbone (N, Cα, C′)	All heavy atoms	Backbone (N, Cα, C′)	All heavy atoms
9–41 and 9′-41′	0.74	1.27	1.07	1.84
Helices I and I′ (9–22 and 9′-22′)	0.68	1.22	0.98	1.76
Helices II and II′ (28–41 and 28′-41′)	0.52	1.21	0.74	1.74
Helices I or I′ (9–22 or 9′-22′)	0.38	1.04	0.55	1.50
Helices II or II′ (28–41 or 28′-41′)	0.34	1.13	0.48	1.64

(residues −1 to 4) with dihedral angles mostly in the β region of the (ϕ,ψ) space, a turn segment (residues 5–8), a helix-loop-helix structural element (residues 9–22 for helices I or I′, 24–27 for a turn segment, 28–41 for helices II or II′) and a disordered C-terminus (residues 42–44). The secondary structure of RIIα D/D was determined from the coordinates of the ensemble of 24 structures using the program MOLMOL [27]. For both helices I (I′) and II (II′) the beginning of the helices is well defined but the end of the helices shows some variation. Helix I (I′) begins at residue 9 and ends at residues 20–23 in the various structures of the ensemble. A weighted average positioned the C-terminus of helix I (I′) at residue 22. Helix II (II′) starts at residue 28 and ends at residues 39–43 in the various structures of the ensemble. A weighted average positioned the C-terminus of helix II (II′) at residue 41. Thus all helices are well defined in their centers with some fraying at their C-termini.

Analysis of the final ensemble of 24 structures of RIIα D/D with PROCHECK-NMR [28] reveals that 71.7% of residues are found in the most favored region, 25.1% in additionally allowed region, 3.1% in the generously allowed region and 0.1% in the disallowed region of the Ramachandran plot. Similar analysis using only the best defined region (residues 9–41, Table 3) of the final ensemble of the 24 structures of RIIα D/D shows that 82.8% of residues are found in the most favored region, 15.8% in the additionally allowed region, 1.4% in the generously allowed region and 0.0% in the disallowed region of the Ramachandran plot.

The inter-helical angles in the ensemble of the RIIα D/D structures are typical for an X-type four-helix bundle. Specifically, the angle between helices I, I′ is 162° ± 7°, between II, II′ is 146° ± 5°, between I, II (I′, II′) is 127° ± 6°, and between I, II′ (I′, II) is 46° ± 5°. (Inter-helical angle of 0° was assigned to parallel N-C helix vectors.) The structures of RIIα D/D presented here and calculated using initial structures of reasonably well-defined monomers, are in excellent agreement with calculated structures of RIIα D/D using initial structures with random ϕ-, ψ-angles [5].

A summary of the various classes of NOEs is presented in Fig. 3A, the number of the different types of NOEs per residue are categorized as intra-monomer and inter-monomer. The intra-monomer NOEs are further classified as intra-residue, short range sequential, medium range sequential and long range. The per-residue rmsd of the backbone heavy atoms (N, Cα, C′) and all heavy atoms is shown in Fig. 3B. Figure 3C–E shows the calculated angular order parameters [29] for backbone ϕ-, ψ-, and side chain χ_1-dihedral angles, using the ensemble of 24 structures of RIIα D/D. From Fig. 3, the flexibility is apparent for the amino terminal segment, −1 to 8, the C-terminal segment, 42–44, and, to a lesser extent, of the loop segment, 23–27, and the C-terminus of helices I, I′ (residues 21–22) and II, II′ (residue 41). These flexible segments also show lower densities of NOEs per residue, as expected. In addition, Fig. 3F shows the calculated percent solvent accessibility [30] of the best dimer structure of RIIα D/D, and it is compared to the percent solvent accessibility of one of the monomers in the best structure of RIIα D/D. Residues Gln4, Ile5, Pro6, Leu9, Leu12, Leu13, Tyr16, Thr17, Val20, Leu21, Gln24, Leu28, Val29, Asp30, Ala32, Val33, Phe36, Thr37, Leu39, and Arg40 show variable changes in solvent accessibility upon dimer formation, which is consistent with the structural characteristics of RIIα D/D. Most of these residues are in helices I (I′), II (II′), with the exception of Gln4 at the end of the disordered N-terminus, Ile5, Pro6 which are part of the first turn [8] and residues Gln24, Asp27 which are part of the second turn of RIIα D/D.

Figure 4 summarizes the structural characteristics of RIIα D/D using the final ensemble of 24 structures and the best structure. Figure 4A, shows the backbone and the hydrophobic side chains (depicted in green) of the final ensemble of 24 structures of RIIα D/D. Only side chains with hydrophobic character in the region 9–41 are shown, and they are Leu9,12,13,21,28,39, Val18,20,29,33, Phe31,36, Tyr16,35, Thr10,17,37. The RIIα D/D possesses a well-formed hydrophobic core between the two monomers, which contributes to the stability and packing of the dimer. Parallel packing of the aromatic side chains Tyr16, Phe31, Tyr35 and Phe36 and contacts involving the side chains of Leu12, Val20, Leu28, Val29, Val33, Thr37 and Leu39, are observed in the hydrophobic core (Fig. 4A). An additional

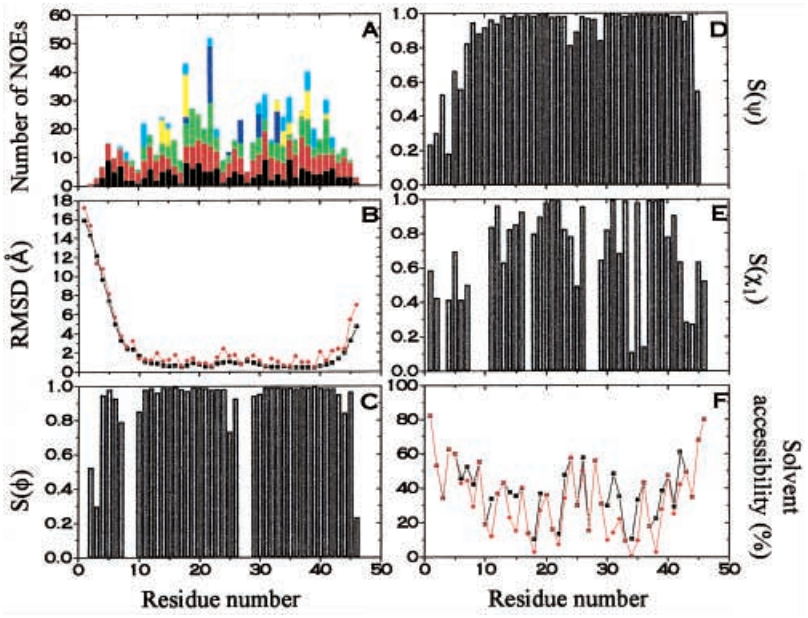

Fig. 3. Structure determination statistics. (A) Number of NOEs per residue for each monomer, used in the dimer structure calculation of RIIα D/D. The NOEs are classified as intraresidue (black), sequential (red), medium range (yellow), long range (green), inter-monomer (blue) and ambiguous (white). (B) Root mean square deviation of the backbone heavy atoms (N, Cα, C′; black squares) and all heavy atoms (red circles) for the ensemble of the 24 lowest energy structures. The 24 structures were fitted using the backbone heavy atoms between residues 9–41. (C–E) Angular order parameters for ϕ-, ψ-, χ_1-dihedral angles, calculated with the method of Hyberts *et al.* [29] using the program MOLMOL [27]. (F) Percent solvent accessibility of the dimer (black squares) and one of the monomers (red circles) of RIIα D/D. In all panels, plotted residue numbers 1–46 correspond to residues −1 to 44, as mentioned in the text.

hydrophobic groove between helices I and I′, partially exposed but with the hydrophobic side chains of Leu9, Leu13, Val18, Leu21 and Thr10, Thr17, packing against each other, is formed outside the protein core. This hydrophobic groove has been identified as the site of interaction with AKAP proteins [5,6]. The symmetry axis of the dimer is along the *y*-axis shown in the Figure. Figure 4B shows the van der Waals model of the top face of the best structure of RIIα D/D in the region −1 to 44. This view is generated by rotating the orientation of RIIα D/D of Fig. 4A by 90° about the *x*-axis (Fig. 4). This view depicts the partially exposed hydrophobic character of the top face of RIIα D/D (the colouring scheme is the same as in Fig. 4A). Interaction of RIIα D/D with AKAP proteins occurs along the hydrophobic interface of the two monomers (Fig. 6B). A further rotation of the orientation of RIIα D/D of Fig. 4B by 180° about the *x*-axis shows the bottom face of RIIα D/D (Fig. 4C). There is some hydrophobic character in the bottom face of RIIα D/D at the monomer interface, which is part of the protein core.

Figure 4D–F shows the ribbon model of the best structure of RIIα D/D in the same orientations as their corresponding left (Fig. 4A–C) and right (Fig. 4G–I) panels. The top (Fig. 4E) and bottom (Fig. 4F) views demonstrate that RIIα D/D forms a typical X-type four-helix bundle structural motif.

Figure 4G shows the backbone and the charged side chains of the final ensemble of 24 structures of RIIα D/D. All positively charged side chains [Arg22,38,40,43,44, His(−1),2] are depicted in blue and all negatively charged side chains (Asp27,30, Glu11,19,34,41) are depicted in red. Figure 4H shows the top face (same as in Fig. 4B,E) of a van der Waals model of the best structure of RIIα D/D. This face is free of charged residues around the interface of the monomers which has been shown to be highly hydrophobic (Fig. 4B), with the exception of Glu11. However, the disordered parts of this face (N- and C-termini) demonstrate the presence of positive charge. Figure 4I shows the bottom face (same as in Fig. 4C) of a van der Waals model of the best structure of RIIα D/D. The central part of this face appears to be highly charged with the presence of both negatively and positively charged residues, symmetrically arranged. Additionally, the disordered N- and C-termini appear to be positively charged.

In our effort to understand the structural properties of the charged face, we have performed pK_a calculations on the ensemble of 24 structures of RIIα D/D. Figure 5 presents a plot of the calculated apparent mean pK_a value per residue and compares them to the model pK_a values of each ionizable site. In addition, Fig. 5 shows the secondary structure of RIIα D/D to aid the analysis. Calculations were performed using the dimer form of RIIα D/D, and the pairs of data points in Fig. 5 correspond to the two monomers. Finally, the error bars reflect the rmsd from the mean pK_a value.

Examination of Fig. 5 reveals that residues located in regions of flexibility (N- and C-termini and inter-helical loop; Fig. 3) tend to have mean pK_a values close to their model pK_a value and with small pK_a rmsd. This is the case for the N-terminus (7.1 ± 0.5), His2 (5.9 ± 0.4), Asp27 (3.4 ± 0.3), Glu41 (4.5 ± 0.3), Arg43 (12.8 ± 0.3), Arg44 (12.7 ± 0.2), and the C-terminus (3.5 ± 0.3), and for residue Arg22 (12.5 ± 0.1), which is located in a well-defined region at the C-terminus of helices I, I′. There is one exception His(−1) which shows a significantly lower mean pK_a value (5.1 ± 0.7) with large variation. This may be attributed to proximity with two basic sites, the N-terminal amide and His2. Aspartic acids Asp27 and Asp30 show lower mean pK_a values than their model pK_a values. This may be a general property of Asp residues, as it has been observed in another study of NMR ensembles of structures [16]. Mean pK_a values of glutamic acids, Glu11 (3.9 ± 0.2) and Glu34 (4.6 ± 0.4), show a small deviation from their model pK_a values and with small variation. However, Glu19 shows an increased mean pK_a value of 5.0 ± 0.4), but with a small variation. Both tyrosines show significantly upshifted mean pK_a values from their model pK_a values with large variations. Indeed the largest shift and variation is observed

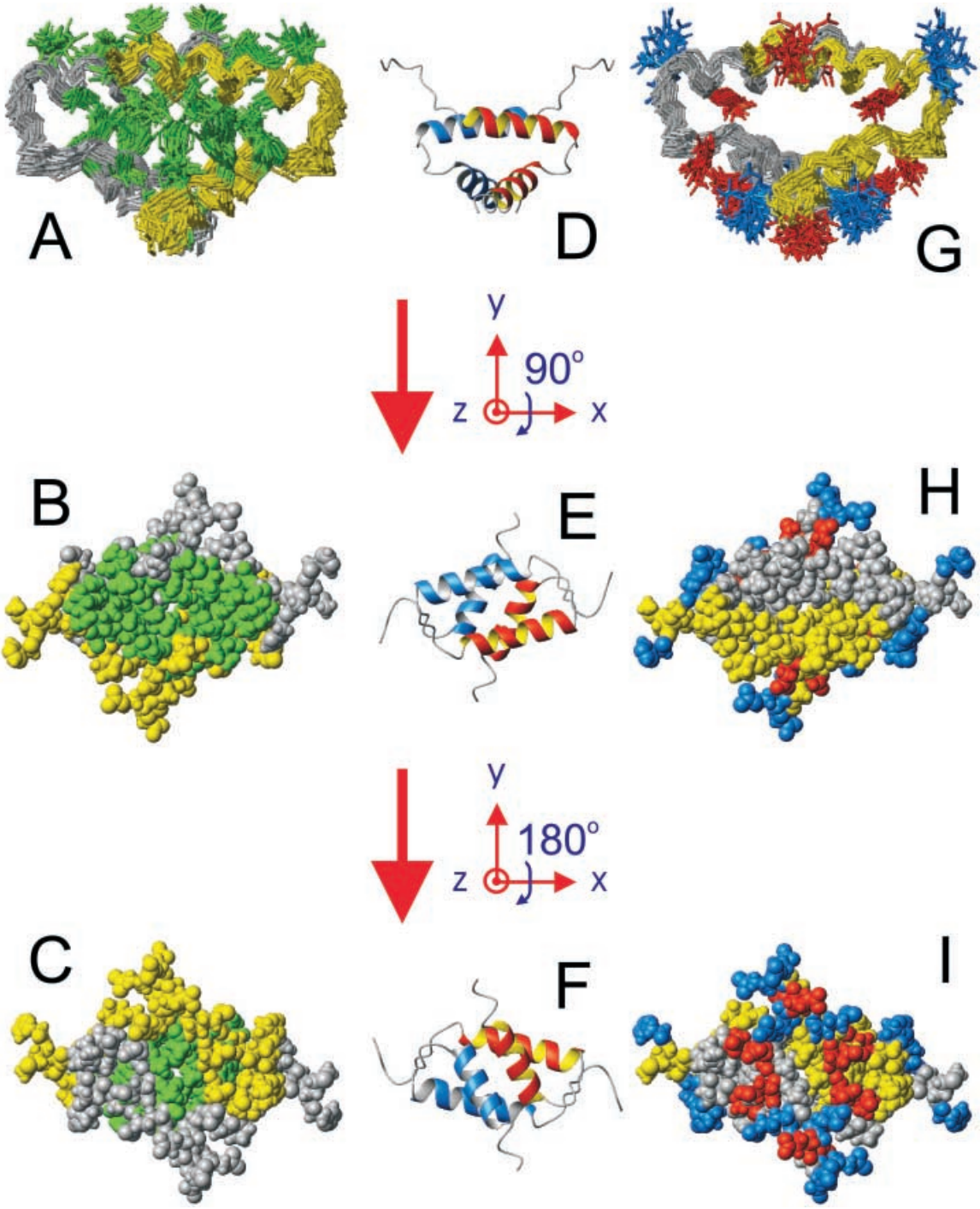

Fig. 4. The hydrophobic and electrostatic character of RIα D/D. (A) A backbone representation of residues 9–41 of the ensemble of the 24 lowest energy structures of RIIα D/D. Only side chains of residues with hydrophobic character (Val, Leu, Ile, Phe, Tyr, Thr) are shown (coloured in green). Monomer 1 is coloured in yellow and monomer 2 is coloured in grey. (B) The top view of a van der Waals sphere model of the best (closest to the mean) structure of RIIα D/D, in an orientation rotated by 90° about the *x*-axis from the orientation of (A). The colours of the two monomers (yellow and grey) and of the hydrophobic residues (green) are as in (A). The dense hydrophobic face (green atoms) is the binding site of the AKAP peptides. (C) The bottom view of a van der Waals sphere model of the best structure of RIIα D/D, in an orientation rotated by 180° about the *x*-axis from the orientation of (B). (D, E, F) Ribbon models of RIIα D/D (residues −1 to 44) in the same orientation as in (A, B, C), respectively. The view in (D) shows the nearly antiparallel arrangement of helices I, I′ and II, II′. Views in (E, F) demonstrate the four-helix bundle structural motif of RIIα D/D. (G) A backbone representation of RIIα D/D (residues 9–41), showing the backbone of the monomers 1 (yellow) and 2 (grey) and charged side chains only. Positively charged side chains (Arg, Lys, His) are shown in blue, and negatively charged side chains (Asp, Glu) are shown in red. This view has the same orientation as in (A) and (D). (H) The top view of a van der Waals sphere representation of RIIα D/D. The orientation of this view is the same as in (B) and (E). (I) The bottom view of a van der Waals sphere representation of RIIα D/D. The orientation of this view is the same as in (C) and (F), and depicts the highly charged bottom face of RIIα D/D. Individual panels in this Figure were generated using the program MOLMOL [27].

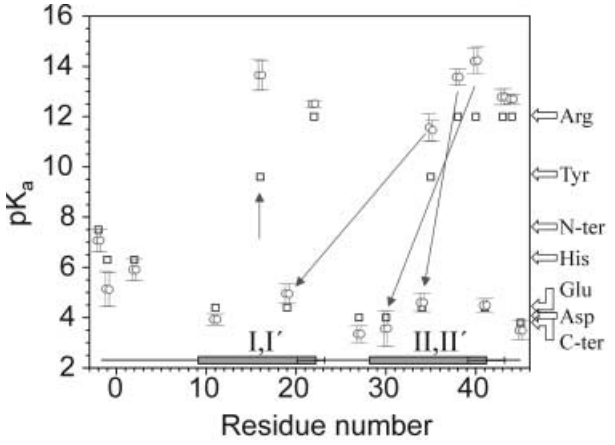

Fig. 5. Plot of the calculated apparent mean pK_a values of ionizable residues of RIIα D/D against the residue number. The model pK_a of each ionizable residue is represented by black open squares. The mean value of the calculated apparent pK_a for each ionizable residue of the ensemble of 24 structures of RIIα D/D, is represented by pairs of grey open circles. The left open circle in each pair corresponds to monomer 1, and right open circle in each pair corresponds to monomer 2. The error bars correspond to root mean square deviations from the mean pK_a value. The arrows depict interactions discussed in text, as follows: intra-helical Arg38–Glu34, inter-helical Tyr35–Glu19, and inter-monomer Arg40–Asp30, and desolvated Tyr16. Note that the studied sample of RIIα D/D contains residues His(−1) and Met0, which have been intorduced by the protein expression system used. Residue −2 in the plot corresponds to the amino terminal ionizable group of His(−1), and residue 45 corresponds to the C-terminal ionizable group of Arg44. The types of ionizable sites corresponding to the model pK_a values are marked on the right hand side of the Figure. The secondary structure of RIIα D/D is shown at the bottom of the figure, with helices depicted as elongated rectangles. Secondary structure has been determined as discussed in text, and the error bar at the C-terminus of each helix corresponds to the variable helical range within the ensemble of the 24 structures. There is no variation at amino terminus of each helix. The sequence of ionizable sites of RIIα D/D is: Nter-His(−1)-His2-Glu11-Tyr16-Glu19-Arg22-Asp27-Asp30-Glu34-Tyr35-Arg38-Arg40-Glu41-Arg43-Arg44-Cter.

for Tyr16 (13.7 ± 0.6). Residue Tyr35 is the only one that shows variation within the two monomers (11.6 ± 0.6 for monomer 1 and 11.5 ± 0.4 for monomer 2; Fig. 5). Finally, the mean pK_a values of residues Arg38 and Arg40, located in the structured region of the charged face, are 13.6 ± 0.3 and 14.2 ± 0.5, respectively.

After examining the NMR structures, we can attribute the upshifted mean pK_a of Tyr16 to desolvation, as there is no other ionizable site within 5 Å of the O_η atom of Tyr16. Tyr16 has < 10% solvent accessibility (Fig. 3F) and is surrounded by residues Gln23, Leu28, Phe31, Phe36 of the same monomer, and Leu9, Leu12, and Leu13 of the other monomer, all but one of them being hydrophobic.

Unfavorable intra-monomer Coulombic interaction between Tyr35 and Glu19 (of the same monomer) explains the upshifted pK_a values of both residues. The distance between Tyr35 (O_η) and Glu19 (smallest distance to $O_{\varepsilon1}$ or $O_{\varepsilon2}$) is 3.6 ± 0.7 Å for the ensemble of structures, and 2.5 Å for the lowest energy structure, which is suggestive of a weak hydrogen bond. The definition of hydrogen bond here is broader and includes not only the distance between the donor and acceptor atoms and their relative orientation, but also the observation of unusual pK_a values attributed to side chain interactions. A dynamic character of the two side chains should also be considered.

The favorable Coulombic interaction of Arg38 with Glu34 within the same monomer and same helix (II or II′), contributes to the high pK_a value of Arg38. The distances between the ionizable sites of Arg38–Glu34 are characteristic of the presence of salt bridges (< 5 Å in 13 structures, and < 6 Å in 17 structures).

In addition, favorable inter-monomer Coulombic interaction of Arg40–Asp30 contributes to the high pK_a values of Arg40 and the low pK_a value of Asp30. The smallest inter-monomer distance between an Arg40 hydrogen donor site (H_ε, $H_{\eta11}$, $H_{\eta12}$, $H_{\eta21}$, $H_{\eta22}$) and an Asp30 acceptor site ($O_{\delta1}$, $O_{\delta2}$) is 3.3 ± 1.6 Å using the ensemble of 24 lowest energy structures, 3.1 ± 1.2 Å using the ensemble of the 23 lowest energy structures, or 2.1 Å using the lowest energy structure of RIIα D/D. (It appears that the 24th lowest energy structure contains a statistical outlier for this particular distance.) These distances are characteristic of an inter-monomer hydrogen bond. Also, an inter-monomer weak salt bridge between Arg40 and Asp27 cannot be excluded, as the smallest inter-monomer distance between a Arg40 hydrogen donor site and an Asp27 acceptor site is < 6 Å in eight out of the 24 lowest energy structures.

DISCUSSION

A four-helix bundle is a common structural motif, which is mainly found as a part of a larger folding unit and, to a lesser extent, as a stand-alone bundle. Several categories of four-helix bundles have been identified, depending on the topology of the four helices, the inter-helical angles and inter-helical distances. RIIα D/D forms a dimeric X-type four-helix bundle with an alternating pattern of nearly antiparallel and nearly orthogonal helix–helix interactions at the dimer interface [31]. We have shown that a finer classification of quaternary structure for dimeric X-type four-helix bundles involves the relative monomer topology. In RIIα D/D the two monomers are packed in a stacked as opposed to an intertwined configuration. Another example of dimeric stand-alone X-type four-helix bundle with symmetry similar to RIIα D/D is the hepatocyte nuclear factor 1α (HNF-1α) [32]; however, the two monomers of HNF-1α are packed into an intertwined configuration. The intertwined monomer packing has also been observed in the *de novo* synthetic four-helix bundle dimeric protein α2D [33]; however, the symmetry of α2D was broken by the introduction of asymmetric mutations. The authors of this study have called the α2D packing 'bisecting U', and have attributed it to the asymmetric inter-helical contacts. In the case of gene regulating protein Arc repressor [34], which forms a stand-alone dimeric four-helix bundle, but with symmetry different from RIIα D/D, a stacked monomer configuration is also formed.

As shown in Fig. 4, dimerization of RIIα D/D is maintained by strong hydrophobic interactions of side chains that form the core of the protein at the dimer interface. The formation of a clustering of side chains within the same monomer and between monomers constitutes the protein hydrophobic core (see Results section; Fig. 4A). The close contacts of Leu13(I)-Leu13(I′) and Phe36(II)-Phe36(II′)

along the symmetry axis of the dimer, bring together helices I, I′ and II, II′, respectively (Fig. 5A), and they are critical for dimerization. This is in agreement with earlier studies where mutations at Leu13 and Phe36 of RIIβ abolish both dimerization and AKAP interaction [35]. This observation supports the hypothesis that noncovalent interactions are sufficient to maintain dimerization. In RIIα there are no disulfide bonds at the dimer interface, as is the case for the RI isoforms [36]. Sequence alignment of the RIα, RIβ, RIIα and RIIβ isoforms reveals the conservation of the strong hydrophobic core, which is essential for the stability of the dimer.

It has been pointed out before [16] that use of NMR structures produce pK_a values with values closer to their experimentally measured pK_a values, when compared with the use of crystallographic structures. These conclusions were reached by performing pK_a calculations on four different proteins with both NMR and crystallographic structures available [16]. In the absence of crystallographic structures of RIIα D/D, we cannot draw similar conclusions. However, we can argue that the availability of an ensemble of NMR structures that agrees with the allowed conformational space without violating the experimentally established restraints, provides a more realistic range of pK_a values within the calculated rmsd, centered around a mean pK_a.

We have performed mean pK_a calculations to assess the involvement of specific electrostatic interactions in stability and packing of RIIα D/D. We have attributed the unusual pK_a shifts of Tyr16, Glu19, Tyr35, Arg38, and Arg40 to Coulombic interactions and desolvation. We have also distinguished side chain interactions that contribute to (a) stability of secondary structure (intra-helical), (b) packing of tertiary structure (intra-monomer, inter-helical), and (c) packing of quaternary structure (inter-monomer, inter-helical).

Intra-helical favorable Coulombic interaction between side chains of Glu34–Arg38 stabilizes the core of each of helices II and II′ through a salt bridge (Fig. 6A). This is in agreement with the fact that the sequence Glu-X-X-X-Arg is a typical helix promoting sequence through ion pair interactions in peptides [37–39]. We do not observe a similar electrostatic interaction contributing to the stability of helices I and I′.

A contribution to the inter-helical packing within each monomer is provided by the interaction between Tyr35 (helix II, II′)-Glu19 (helix I, I′, close to C-terminus), which is suggestive of a weak intra-monomer and inter-helical hydrogen bond (Fig. 6B). Interestingly, this hydrogen bond is not observed in the rejected top-bottom structures. It is possible that the inter-helical contact of Tyr35 and Glu19 is an essential condition for the distinction of the stacked top-top vs. the intertwined top-bottom relative monomer topology. It is also possible that in X-type four helix bundles where the tertiary and quaternary packing is exclusively hydrophobic, without the presence of an inter-helical hydrogen bond, an intertwined top-bottom monomer arrangement may be more favorable.

In the case of the symmetric homodimer HNF-1α structure, which consists of intertwined monomers, inter-helical interactions between a residue close to the C-terminus of helix I (I′) and a residue in the middle of helix II (II′), is absent. The transcription regulation protein ROP forms a dimeric stand-alone four-helix bundle with

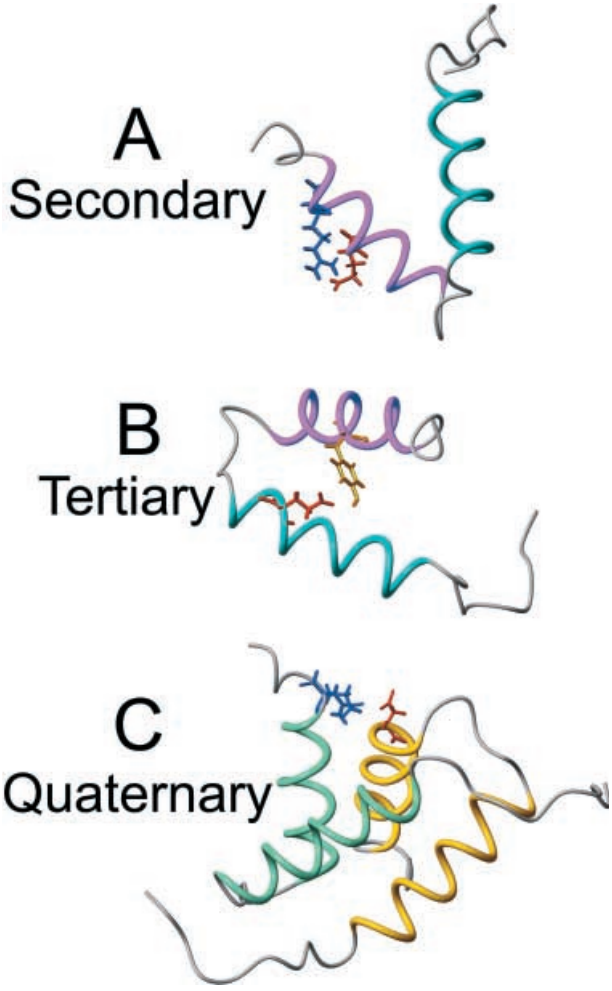

Fig. 6. Electrostatic interactions contributing to the stability of RIIα D/D. (A) Molecular representation of intra-monomer, intra-helical salt bridge between side chains of Arg38 (in blue)–Glu34 (in red), which stabilizes helix II or II′ secondary structure. (B) Side chain intra-monomer, inter-helical weak hydrogen bond Tyr35 (in yellow)–Glu19 (in red), which stabilizes tertiary structure. In both (A) (B) only one monomer is shown for clarity, with helix I drawn in cyan and helix II drawn in magenta. (C) Inter-monomer hydrogen bond between side chains of Arg40 (in blue)–Asp30 (in red), which stabilizes quaternary structure. The two monomers are drawn in yellow and green, respectively. Only one pair of Arg40-Asp30 is shown for clarity.

all-antiparallel helix geometry and stacked monomer configuration [40]. Introduction of a single Ala to Pro mutation in the inter-helical loop of each monomer in ROP is sufficient to change the quaternary structure to an intertwined monomer configuration [41]. Also, excision of the inter-helical loop results to a totally different packing and oligomerization state [42]. It is possible that the stability of the inter-helical loop in RIIα D/D is a crucial factor in discriminating the packed from the intertwined monomer arrangement. The Tyr35–Glu19 inter-helical interaction may be contributing in the conformational state of the inter-helical loop in RIIα D/D.

It is possible that the alternative packing observed on the ensemble of the five rejected top-bottom structures of RIIα D/D occurs because of differences in the conformation of

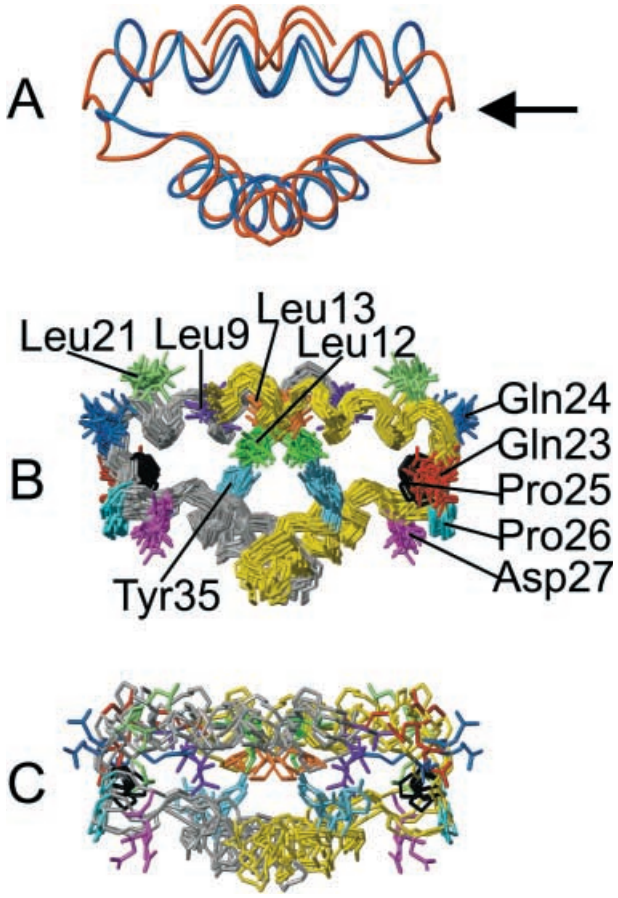

Fig. 7. Comparison of the ensembles of top-top and top-bottom structures. (A) Tube representation of the lowest energy structures of the top-top ensemble (red) and the top-bottom ensemble (blue) in the ordered region between residues 9–41. The arrow points to inter-helical loop differences discussed in text. (B) Superposition of the backbone of the 24 accepted structures that form the top-top ensemble using the ordered region between residues 9–41. (C) Superposition of the backbone of the five rejected structures that form the top-bottom ensemble using the ordered region between residues 9–41. In both (B) and (C), selected hydrophobic side chains, Leu9 (purple), Leu12 (green), Leu13 (orange), Leu21 (light green), and Tyr35 (light blue) that show significant conformational differences in the two ensembles, and all five residues of the inter-helical loop, Gln23 (red), Gln24 (blue), Pro25 (black), Pro26 (cyan), Asp27 (magenta) are drawn, while all other side chains have been deleted for clarity. The backbone of monomer 1 is coloured in yellow and of monomer 2 is coloured in grey. The superpositions of structures were made by fitting the coordinates of the backbone heavy atoms (N, Cα, C′). The Figure was generated using the program MOLMOL [27].

the loop connecting helices I and II (I′ and II′). Figure 7A shows a superposition of the lowest energy structures from the ensembles of the 24 accepted top-top structures and the five rejected top-bottom structures, respectively. The conformations of the inter-helical loop differ significantly in the two structures. Figure 7B,C shows superpositions of the 24 top-top and the five top-bottom structures, respectively, depicting loop residues Gln23, Gln24, Pro25, Pro26, Asp27, and selected hydrophobic residues that show significant conformational differences in the two ensembles. The backbone torsion angles of Gln24 and the side chain torsion angles of both Gln23 and Gln24 are significantly different in the two ensembles, while the remaining three residues of the loop do not show conformational differences. If interactions between helices and turns are important for quaternary packing, these loop differences can explain the variation in the packing of the two ensembles. The inter-helical angle between I-II (I′-II′) is smaller in the top-bottom ensemble, while the inter-helical angles between I-I′ and II-II′ are larger in the top-bottom ensemble (values: 118° ± 10°, 127° ± 6° for I-II; 170° ± 4°, 162° ± 7° for I-I′; 159° ± 7°, 146° ± 5° for II-II′, where the first value corresponds to the top-bottom and the second value to the top-top ensemble). These differences are associated with a tighter hydrophobic packing in a congested smaller core in the top-bottom structures, which has resulted in a different packing of the hydrophobic side chains (especially of Leu9, Leu12, Leu13, Leu21, and Tyr35; Fig. 7B,C) and in the observed experimental restraint violations. It is worth noting the switch of Leu13 from being part of the exposed hydrophobic groove in the top-top structures to becoming part of the hydrophobic core in the top-bottom structures and assuming the role of neighboring Leu12 in participating in the formation of the hydrophobic core (Fig. 7B,C). In addition, the calculated percent solvent accessibility for loop residues Gln23 and Gln24 using the ordered region between residues 11–43, is significantly reduced in the top-bottom compared to the top-top ensemble, contributing to energetically less favorable conformations of the polar side chains of Gln23 and Gln24 in the top-bottom compared to the top-top structure. These observations, together with the experimental restraint violations, suggest that the top-bottom structure would be of lower stability and therefore is not found in the native protein. It would be interesting to see if mutating residues in the loop region would affect quaternary packing, as is the case for ROP [41]. Ongoing work will address this question.

We have pointed out above the presence of hydrophobic contacts between helices I, I′ and II, II′, which are important for packing and dimerization. The antiparallel arrangement of the NH-CO vectors of helices I, I′ or II, II′, is an optimal alignment for the helix dipoles. This alignment gives some electrostatic character in the otherwise hydrophobic packing and stability of helices I, I′. Additional quaternary packing interactions of electrostatic character are the observed favorable inter-monomer Coulombic interactions between Arg40 of helix II (II′) of one monomer with Asp30 of helix II′ (II) of the other monomer. The Arg40–Asp30 interaction is suggestive of the presence of an inter-monomer hydrogen bond. Finally, the very high pK_a value of Tyr16 can only be attributed to a highly desolvated environment, contributed by hydrophobic residues from both monomers. The role that Tyr16 plays in the structure of RIIα D/D is not yet understood.

RIIα D/D possesses two diametrically opposed functional faces, one highly hydrophobic (top face, Fig. 4A,B) and one highly charged (bottom face, Fig. 4G,I), located at exactly opposite directions. The N-terminal face contains a highly hydrophobic groove (Fig. 4B) along the solvent exposed part of the interface of helices I, I′ (Fig. 4A). This is an unusual but very significant characteristic of RIIα D/D, which promotes participation in protein–protein interactions and in mediating intracellular signal transduction events. The hydrophobic side chains of this groove cluster

against each other and they are clearly independent from the protein hydrophobic core. The exposed hydrophobic groove is the binding site of the amphipathic AKAP peptides through their hydrophobic face. This observation is supported by structure determination of the complex RIIα D/D with AKAP peptides Ht31(493–515) and AKAP79(392–413) [6] and with a peptide docking model [5], which showed the alignment of the exposed hydrophobic groove of RIIα D/D with the hydrophobic surface of the AKAP peptides.

The C-terminal face is a highly charged surface with symmetrically arranged charged residues. The charged face of RIIα D/D contains residues Asp27, Asp30, Glu34, Arg38, Arg40, Glu41, Arg43, and Arg44, of which Arg42 and Arg44 are located in the disordered end. A recent study on the flexibility of the full length regulatory subunit of free RIα isoform and complexed with the catalytic subunit, using fluorescence anisotropy [43] has shown that there is a short flexible segment at the C-terminal site of the dimerization and docking domain. This could allow the interdomain/cAMP binding region to pivot about the stable AKAP-bound dimerization and docking domain, and to weakly associate with another part of the molecule, possibly the tandem cAMP binding domains of the regulatory subunit [43]. This association becomes strong when the catalytic subunit is bound, while allowing the autoinhibitory sequence of the interdomain to slip into the active site cleft of the catalytic subunit to inhibit its activity [43]. In addition, a low resolution solution structure of PKA holoenzyme by neutron contrast variation, has suggested two potentially interconverting structural models through a hinge movement at the intersection of the RIIα subunit and the autoinhibitory sequence [44]. The presence of the charges in the C-terminal face of RIIα D/D may be essential to provide flexibility for the transition of the inactive holoenzyme (with bound catalytic subunit) to active form (with free catalytic subunit), upon cAMP binding in the regulatory subunit. It is possible that in the activated form of the regulatory subunit, the charges of the C-terminal face of RIIα D/D participate in interactions with phosphorylation sites of the regulatory subunit, which are of the type Arg/Lys-Arg-X-Ser/Thr or with the arginine-rich autoinhibitory sequence. It is also possible that the C-terminal face stabilizes other protein–protein interactions. This is the subject of current investigation. Also, mapping studies to determine a potential site of interaction between RIIα D/D with other parts of the regulatory subunit and the catalytic subunit are currently in progress, with the hope that they might shed light into the importance of the intriguing, highly charged, face of RIIα D/D.

Coordinates

Coordinates of the ensemble of 24 structures of RIIα D/D have been deposited with the Protein Data Bank under accession no. 1L6E. Note, that residue numbering in the coordinate file runs from 1 to 46 instead of −1 to 44 as it is presented here. This is to account for the first two residues [His(−1), Met0], which are added as consequence of the construction of the protein expression system.

ACKNOWLEDGEMENTS

This work was supported in part by National Institutes of Health Grants DK54441 (P. A. J. and J. D. S.), GM19879 and DK07233 (D. M.), CA09523 (M. R.), GM07313 (MGN), the Cancer Research Coordinating Center (P. A. J.), the American Cancer Society (P. A. J.), and American Heart Association Grant 97–425 (M. G. N.). We gratefully acknowledge Drs Sean O'Donoghue for helpful discussions, Andrew McCammon for providing us with UHBD, Gert Vriend and Jens Nielsen for providing us with a special version of WHAT IF, and Joseph Adams, for his critical reading of this manuscript.

REFERENCES

1. Schillace, R.V. & Scott, J.D. (1999) Organization of kinases, phosphatases, and receptor signaling complexes. *J. Clin. Invest.* **103**, 761–765.
2. Edwards, A.S. & Scott, J.D. (2000) A-kinase anchoring proteins: protein kinase A and beyond. *Curr. Opin. Cell Biol.* **12**, 217–221.
3. Dell'Acqua, M.L. & Scott, J.D. (1997) Protein kinase A anchoring. *J. Biol. Chem.* **272**, 12881–12884.
4. Huang, L.J., Durick, K., Weiner, J.A., Chun, J. & Taylor, S.S. (1997) Identification of a novel protein kinase A anchoring protein that binds both type I and type II regulatory subunits. *J. Biol. Chem.* **272**, 8057–8064.
5. Newlon, M.G., Roy, M., Morikis, D., Hausken, Z.E., Coghlan, V., Scott, J.D. & Jennings, P.A. (1999) The molecular basis of protein kinase A anchoring revealed by solution NMR. *Nat. Struct. Biol.* **6**, 222–227.
6. Newlon, M.G., Roy, M., Morikis, D., Carr, D.W., Westphal, R., Scott, J.D. & Jennings, P.A. (2001) A novel mechanism of PKA anchoring revealed by solution structures of anchoring complexes. *EMBO J.* **20**, 1651–1662.
7. Keryer, G., Yassenko, M., Labbé, J.-C., Castro, A., Lohmann, S.M., Evain-Brion, D. & Taskén, K. (1998) Mitosis-specific phosphorylation and subcellular redistribution of the RIIα regulatory subunit of cAMP-dependent protein kinase. *J. Biol. Chem.* **273**, 34594–34602.
8. Newlon, M.G., Roy, M., Hausken, Z.E., Scott, J.D. & Jennings, P.A. (1997) The A-kinase anchoring domain of type IIα CAMP-dependent protein kinase is highly helical. *J. Biol. Chem.* **272**, 23637–23644.
9. Brünger, A.T., Clore, G.M., Gronenborn, A.M. & Karplus, M. (1986) Three-dimensional structure of proteins determined by molecular dynamics with interproton distance restraints: Application to crambin. *Proc. Natl Acad. Sci. USA* **83**, 3801–3805.
10. Nilges, M. (1993) A calculation strategy for the structure determination of symmetric dimers by ^{1}H NMR. *Prot. Struct. Funct. Genet.* **17**, 297–309.
11. Brünger, A.T. (1992) *X-PLOR*. Yale University Press, New Haven, CT.
12. Nilges, M., Clore, G.M. & Gronenborn, A.M. (1988) Determination of three-dimensional structures of proteins form interproton distance data by hybrid distance geometry-dynamical simulated annealing calculations. *FEBS Lett.* **229**, 317–324.
13. O'Donoghue, S.I., King, G.F. & Nilges, M. (1996) Calculation of symmetric multimer structures from NMR data using a priori knowledge of the monomer structure, co-monomer restraints, and interface mapping: The case of leucine zippers. *J. Biomolec. NMR* **8**, 193–206.
14. O'Donoghue, S.I. & Nilges, M. (1999) Calculation of symmetric oligomer structures from NMR data. In *Biological Magnetic Resonance: Structure Computation and Dynamics in Protein NMR*, **Vol. 17** (Krishna, N.R. & Berliner, J.L., eds) pp. 131–161. Plenum Publishers, New York.
15. Antosiewicz, J., McCammon, J.A. & Gilson, M.K. (1994) Prediction of pH-dependent properties of proteins. *J. Mol. Biol.* **238**, 415–436.
16. Antosiewicz, J., McCammon, J.A. & Gilson, M.K. (1996) The determinants of pK_as in proteins. *Biochemistry* **35**, 7819–7833.

17. Madura, J.D., Davis, M.E., Gilson, M.K., Wade, R.C., Luty, B.A. & McCammon, J.A. (1994) Biological applications of electrostatic calculations and brownian dynamics simulations. *Rev. Comput. Chem.* **5**, 229–267.
18. Madura, J.D., Briggs, J.M., Wade, R.C., Davis, M.E., Luty, B.A., Ilin, A., Antosiewicz, J., Gilson, M.K., Bagheri, B., Scott, L.R. & McCammon, J.A. (1995) Electrostatics and diffusion of molecules in solution – simulations with the University of Houston Brownian Dynamics Program. *Comput. Phys. Commun.* **91**, 57–95.
19. Gilson, M.K. (1993) Multiple-site titration and molecular modelling: two rapid methods for computing energies and forces for ionizable groups in proteins. *Prot. Struct. Funct. Genet.* **15**, 266–282.
20. Davis, M.E. & McCammon, J.A. (1990) Electrostatics in biomolecular structure and dynamics. *Chem. Rev.* **90**, 509–521.
21. Gilson, M.K., Davis, M.E., Luty, B.A. & McCammon, J.A. (1993) Variational analysis of and numerical calculation of atomic forces for the Poisson–Boltzmann equation by the method of finite differences. *J. Phys. Chem.* **97**, 3591–3600.
22. Gilson, M.K. & Honig, B. (1988a) Calculation of the total electrostatic energy of a macromolecular system: solvation energies, binding energies, and conformational analysis. *Prot. Struct. Funct. Genet.* **4**, 7–18.
23. Gilson, M.K. & Honig, B.H. (1988b) Energetics of charge–charge interactions in proteins. *Prot. Struct. Funct. Genet.* **3**, 32–52.
24. Sitkoff, D., Sharp, K.A. & Honig, B. (1994) Accurate calculation of hydration free energies using macroscopic solvent models. *J. Phys. Chem.* **98**, 1978–1988.
25. Nielsen, J.E., Andersen, K.V., Honig, B., Hooft, R.W., Klebe, G., Vriend, G. & Wade, R.C. (1999) Improving macromolecular electrostatics calculations. *Protein Eng.* **12**, 657–662.
26. Vriend, G. (1990) WHAT IF: a molecular modeling and drug design program. *J. Mol. Graph.* **8**, 52–56.
27. Koradi, R., Billeter, M. & Wüthrich, K. (1996) MOLMOL: a program for display and analysis of macromolecular structures. *J. Mol. Graphics* **14**, 51–55.
28. Laskowski, R.A., Rullmann, J.A., MacArthur, M.W., Kaptein, R. & Thornton, J.M. (1996) AQUA and PROCHECK-NMR: programs for checking the quality of protein structures solved by NMR. *J. Biomolec. NMR* **8**, 477–486.
29. Hyberts, S.G., Goldberg, M.S., Havel, T.F. & Wagner, G. (1992) The solution structure of eglin c based on measurements of many NOEs and coupling constants and its comparison with X-ray structures. *Protein Sci.* **1**, 736–751.
30. Lee, B. & Richards, F.M. (1971) The interpretation of protein structures: estimation of static solvent accessibility. *J. Mol. Biol.* **55**, 379–400.
31. Harris, N.L., Presnell, S.R. & Cohen, F.E. (1994) 4-Helix bundle diversity in globular-proteins. *J. Mol. Biol.* **236**, 1356–1368.
32. Rose, R.B., Endrizzi, J.A., Cronk, J.D., Holton, J. & Alber, T. (2000) High-resolution structure of the HNF-1α dimerization domain. *Biochemistry* **39**, 15062–15070.
33. Hill, R.B. & DeGrado, W.F. (1998) Solution structure of α_2D, a nativelike *de novo* designed protein. *J. Am. Chem. Soc.* **120**, 1138–1145.
34. Bonvin, A.M., Vis, H., Breg, J.N., Burgering, M.J., Boelens, R. & Kaptein, R. (1994) Nuclear magnetic resonance solution structure of the Arc repressor using relaxation matrix calculations. *J. Mol. Biol.* **236**, 328–341.
35. Li, Y. & Rubin, C.S. (1995) Mutagenesis of the regulatory subunit (RIIα) of cAMP-dependent protein kinase IIβ reveals hydrophobic amino acids that are essential for RIIβ dimerization and/or anchoring RIIβ to the cytosceleton. *J. Biol. Chem.* **270**, 1935–1944.
36. Leon, D.A., Herberg, F.W., Banky, P. & Taylor, S.S. (1997) A stable alpha-helical domain at the N terminus of the RI alpha subunits of cAMP-dependent protein kinase is a novel dimerization/docking motif. *J. Biol. Chem.* **272**, 28431–28437.
37. Marqusee, S. & Baldwin, R.L. (1987) Helix stabilization by Glu^{-}… Lys^{+} salt bridges in short peptides of de novo design. *Proc. Natl Acad. Sci. USA* **84**, 8898–8902.
38. Merutka, G. & Stellwagen, E. (1991) Effect of amino acid ion pairs on peptide helicity. *Biochemistry* **30**, 1591–1594.
39. Merutka, G., Morikis, D., Bruschweiler, R. & Wright, P.E. (1993) NMR evidence for multiple conformations in a highly helical model peptide. *Biochemistry* **32**, 13089–13097.
40. Banner, D.W., Kokkinidis, M. & Tsernoglou, D. (1987) Structure of the ColE1 Rop protein at 1.7 Å resolution. *J. Mol. Biol.* **196**, 657–675.
41. Glykos, N.M., Cesareni, G. & Kokkinidis, M. (1999) Protein plasticity to the extreme: changing the topology of a 4-α-helical bundle with a single amino acid substitution. *Structure* **7**, 597–603.
42. Lassalle, M.W., Hinz, H.-J., Wenzel, H., Vlassi, M., Kokkinidis, M. & Cesareni, G. (1998) Dimer-to-tetramer transformation: loop excision dramatically alters structure and stability of the ROP four α-helix bundle protein. *J. Mol. Biol.* **279**, 987–1000.
43. Li, F., Gangal, M., Jones, J.M., Deich, J., Lovett, K.E., Taylor, S.S. & Johnson, D.A. (2000) Consequences of cAMP and catalytic subunit binding on the flexibility of the A-kinase regulatory subunit. *Biochemistry* **39**, 15626–15632.
44. Zhao, J., Hoye, E., Boylan, S., Walsh, D.A. & Trewhella, J. (1998) Quaternary structures of a catalytic subunit-regulatory subunit dimeric complex and the holoenzyme of the cAMP-dependent protein kinase by neutron contrast variation. *J. Biol. Chem.* **273**, 30448–30459.